arXiv:1409.7768v1 [cond-mat.mes-hall] 27 Sep 2014

Topological Effects on the Magnetoconductivity in Topological Insulators

Vincent E. Sacksteder IV[1*] and Kristin Bjorg Arnardottir
Division of Physics and Applied Physics, Nanyang Technological University, 21 Nanyang Link, Singapore 637371

Stefan Kettemann
Division of Advanced Materials Science, Pohang University of Science and Technology (POSTECH), Pohang 790-784, South Korea and School of Engineering and Science, Jacobs University Bremen, Bremen 28759, Germany

Ivan A. Shelykh
Division of Physics and Applied Physics, Nanyang Technological University, 21 Nanyang Link, Singapore 637371 and Science Institute, University of Iceland, Dunhagi-3, IS-107, Reykjavik, Iceland

(Dated: September 30, 2014)

Three-dimensional strong topological insulators (TIs) guarantee the existence of a 2-D conducting surface state which completely covers the surface of the TI. The TI surface state necessarily wraps around the TI's top, bottom, and two sidewalls, and is therefore topologically distinct from ordinary 2-D electron gases (2DEGs) which are planar. This has several consequences for the magnetoconductivity $\Delta\sigma$, a frequently studied measure of weak antilocalization which is sensitive to the quantum coherence time τ_ϕ and to temperature. We show that conduction on the TI sidewalls systematically reduces $\Delta\sigma$, multiplying it by a factor which is always less than one and decreases in thicker samples. In addition, we present both an analytical formula and numerical results for the tilted-field magnetoconductivity which has been measured in several experiments. Lastly, we predict that as the temperature is reduced $\Delta\sigma$ will enter a wrapped regime where it is sensitive to diffusion processes which make one or more circuits around the TI. In this wrapped regime the magnetoconductivity's dependence on temperature, typically $1/T^2$ in 2DEGs, disappears. We present numerical and analytical predictions for the wrapped regime at both small and large field strengths. The wrapped regime and topological signatures discussed here should be visible in the same samples and at the same temperatures where the Altshuler-Aronov-Spivak (AAS) effect has already been observed, when the measurements are repeated with the magnetic field pointed perpendicularly to the TI's top face.

PACS numbers: 73.20.Fz, 73.43.Qt , 73.23.-b, 73.25.+i

I. INTRODUCTION

The hallmark of topological insulators (TIs) is metallic transport on their surfaces, coexisting with and reinforced by an insulating bulk.[1–6] In diffusive samples where the scattering length is smaller than the sample size, the TI surface state's conductivity is predicted to increase in the presence of scattering due a quantum interference phenomenon called weak antilocalization (WAL).[7–10] The weak antilocalization is destroyed if time reversal symmetry is broken, so a small perpendicular magnetic field is sufficient to cause a clear drop in a TI's conductivity.[11,12] This negative magnetoconductivity at small fields is both the most accessible and the most frequently measured signal of weak antilocalization in TIs. The magnetoconductivity profile has a universal shape described in Hikami, Larkin, and Nagaoka's (HLN) celebrated paper, and frequently observation of this signal is used as a diagnostic determining the presence of 2-D surface transport.[13]

The HLN formula was derived for a 2-D electron gas (2DEG) moving on an infinite plane. In an infinitely extended TI slab there would be two 2DEG layers, one on the TI's top and the other on the bottom. If the top and bottom are decoupled then both the TI's conductance G and its conductivity $\sigma = GL/W$ will simply be twice the HLN result, while if they are tightly coupled the doubling will be absent. (L and W are the sample length and width.) This simple prescription for doubling the HLN magnetoconductivity has been confirmed by experiments on TI films which varied the coupling between the top and bottom surfaces.[14–16]

This prediction suffers, however, from ignoring the structure of the topological insulator's surface state. Any strong TI sample is completely enfolded by its surface state, as guaranteed by topological protection. In particular, the surface state occupies not only the TI's top and bottom, but also its sidewalls. All of the TI's surfaces are coupled to each other, in contradiction to the simplistic HLN picture. Therefore the finite TI sample size cannot be pushed to infinity, and must have an important role in the magnetoconductivity. The current paper is devoted to a detailed investigation of the corresponding effects.

We will will start from consideration of a TI surface state that wraps the entire sample and we will compute the perpendicular magnetoconductivity including the top, bottom, and sidewalls. We will show that the sidewalls always cause a reduction of the conductivity with respect to the prediction of the HLN formula, because a perpendicular magnetic field does not destroy

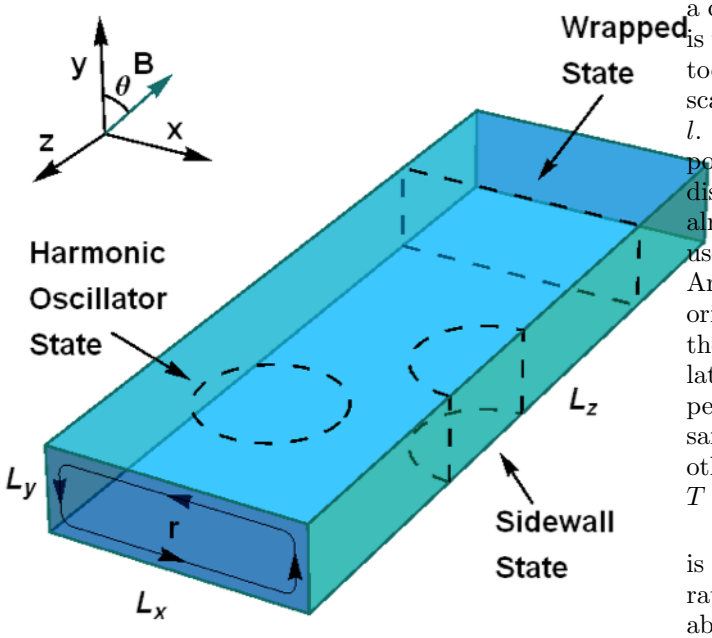

FIG. 1: (Color online.) The TI sample geometry and typical Weak Antilocalization states. This article studies a TI sample of width L_x and height L_y. Conduction is along the z axis, and the magnetic field B is in the $x-y$ plane. "Perpendicular" fields are parallel to the y axis and perpendicular to the sample's top face, with $\theta = 0$. "In-plane" fields are parallel to the x axis, with $\theta = \pi/2$. We use an r coordinate which wraps the TI sample's perimeter, as shown by the arrowed line making a circuit around the front face. The dashed lines illustrate three kinds of weak antilocalization states which contribute to the magnetoconductivity. The Harmonic Oscillator WAL states execute cyclotron motion on a single face, the Sidewall states execute plane wave motion on the sidewalls and reflect off the top and bottom faces, and the Wrapped states make circuits around the entire TI perimeter.

quantum interference processes which occur on the sidewalls. This result will modify the interpretation of experimental measurements of the magnetoconductivity signal's magnitude, which is used as a diagnostic determining whether a TI sample's surfaces are strongly coupled.

A more intriguing result occurs when quantum phase coherence survives long enough to allow a diffusing charge to make a circuit around the sample, i.e. when the diffusive coherence length L_ϕ is comparable to the sample perimeter L_r. In this regime the magnetoconductivity is dominated by quantum interference between the paths making one or more turns around the sample, and the HLN formula must be completely replaced. In contrast with the HLN formula's prediction that the magnetoconductivity is governed by L_ϕ, in this wrapped regime the TI magnetoconductivity at low fields is controlled by the sample width L_x. The most distinctive signature of this effect is that $\sigma(B)$ will lose its temperature dependence, differently from the HLN formula which scales with T^{-2}. The transition from wrapped to HLN behavior occurs at a characteristic field strength $eB_w/\hbar = (4L_x l)^{-1}$ where l is the scattering length. It is remarkable that the magnetoconductivity, a result of diffusive physics at long length scales, is sensitive to the small scattering length scale l. This is a consequence of equipartition of kinetic and potential energy in each Landau level state, as we will discuss later. The $L_r \leq L_\phi$ regime discussed here has already been achieved in those experiments which have used a longitudinal magnetic field to observe Altshuler-Aronov-Spivak (AAS) oscillations; all that is needed is to orient the field perpendicularly to the sample and repeat the magnetoconductivity measurement.[17,18] AAS oscillations have been reported at $T = 2\ K$ in samples with perimeters L_r as large as $500\ nm$, indicating that in those samples L_ϕ reached or exceeded the same value.[19–21] Another experiment reported that L_ϕ exceeded 2 microns at $T = 60\ mK$.[22]

We will also report on the case when the magnetic field is oriented in-plane so that it pierces the TI sidewalls rather than the top and bottom. All previous theory about the in-plane magnetoconductivity treated quantum wells where the charge carriers move freely between the top and bottom surfaces, or attributed it to the TI surface state's penetration into or through the bulk.[23–27] In-plane signals in TIs sometimes have been attributed to the bulk contribution to conduction in the TI sample.[28,29] Here we show that the TI sidewalls are also a natural explanation of in-plane observations in TIs. In this case the sample height L_y, not the penetration depth λ, controls the in-plane effect, consistently with at least one recent experiment.[30]

Lastly we report analytical and numerical results on tilted fields (i.e. when the field orientation makes an arbitrary angle θ between the perpendicular and in-plane directions.) The corresponding measurements have been used as diagnostics to confirm that the observed magnetoconductivity is sensitive only to $B\cos\theta$, not B and $\cos\theta$ separately, as expected for a 2-D electron gas.[14,28,29,31–35] Most experiments find good agreement with the 2-D expectation only at small fields and small angles.[28,29,33,35] Some experiments have attributed the in-plane signal to the bulk and simply subtracted it from their results at other angles[28,29], while one detailed experiment showed that this procedure could not match observations.[31] Here we present graphs of the magnetoconductivity corresponding to the tilted field results that experimentalists might expect to obtain and propose an approximate interpolating formula.

The structure of this article is as follows. In Section II we will review the HLN formula for perpendicular fields and several results for in-plane fields, because these results are widely used and will be our reference points. Next section III introduces our model, explains our method for evaluating the magnetoconductivity numerically, and details the important parameters and length scales. Section IV presents and discusses our numerical results, and we summarize our conclusions in section V. The Appendix presents certain analytical re-

sults on the magnetoconductivity.

II. OVERVIEW OF THE RESULTS FOR 2-D ELECTRON GASES

For magnetic fields perpendicular to a 2-D electron gas, the Hikami-Larkin-Nagaoka (HLN) formula has proved to give an adequate description of numerous experimental results. The TI surface is a spin-1/2 system with strong spin orbit coupling, and spin polarization decays very quickly so only the spin singlet channel participates in diffusive conduction.[36] In this case the HLN formula reads:

$$\begin{aligned}\sigma_{HLN}(x) &= \sigma(B=0) \\ &+ \alpha\frac{G_0}{2\pi}(\psi(1/2+E_l/x)-\psi(1/2+1/x))\end{aligned} \quad (1)$$

where $G_0 = 2e^2/h$ is the conductance quantum, $\psi(x)$ is the digamma function, and $\alpha = 1/2$ sets the magnitude. $L_B = \sqrt{\hbar/2eB}$ is the magnetic length controlling quantum interference in a magnetic field, and the parameter $x = 2L_\phi^2/L_B^2$ is proportional to the magnetic field strength B. $L_\phi = \sqrt{D\tau_\phi}$ is the average distance that an electron covers before dephasing kills the corresponding quantum interference diagrams, and D is the diffusion constant. τ_ϕ is the dephasing time, which typically scales with T^{-1} in 2-D diffusive systems and is sensitive to the dimensionality. The short-wavelength, high-energy cutoff on quantum interference processes is given by $E_l = L_\phi^2/l^2$, where l is the scattering length.

At small B (i.e. $L_B \gg L_\phi$) the HLN formula is a quadratic $\sigma_{HLN} \approx -\alpha\frac{G_0}{2\pi}\frac{x^2}{24}$. It displays a shoulder at $L_B \propto L_\phi$ and transitions to a logarithmically decreasing curve at high fields. At small fields σ_{HLN} is typically proportional to T^{-2}, at large fields it scales with $\ln T$, and the shoulder occurs at a value of B which typically scales with T.

Experimental fits to the HLN formula focus on three parameters:

- Many experiments focus on $\sigma(B)$ at small fields where it is quadratic. They measure the coefficient b of the quadratic term, i.e. the coefficient b of $\sigma_{HLN} = -\alpha\frac{G_0}{2\pi} \times bB^2$. The HLN formula predicts that $b = 2e^2L_\phi^4/3\hbar^2$.

- Using data at higher fields it is possible to measure the diffusion length $L_\phi = \sqrt{D\tau_\phi}$, which determines the position of the HLN shoulder. Since only τ_ϕ and not D depends on temperature, magnetoconductivity measurements are a good probe of dephasing and its sources.

- At higher fields one can also measure the magnitude α. If one plots $\sigma(B)$ as a function of $\ln B$, one should obtain a straight line for large B. The slope determines α. The HLN formula fixes α unambiguously at $\alpha = 1/2$ for a single 2DEG with strong spin-orbit coupling. However experimentally α is observed to vary continuously in TI samples and to have values as large as 1 (or even larger[15]), and this has been attributed to the TI's top and bottom surfaces.

Several authors have generalized the HLN formula to a pair of 2DEGs linked by random (disordered) jumps from one layer to the other, similarly to an infinite TI slab with no side surfaces.[16,27,37] This model adds an extra time scale τ_c characterizing the average time between interlayer jumps. Its behavior is strongly dependent on the ratio τ_c/τ_ϕ and on the coupling length scale $L_c = L_\phi\sqrt{\tau_c/\tau_\phi}$. The exact result is the sum of two HLN curves σ_a and σ_b. In the weakly coupled $\tau_c/\tau_\phi \gg 1$ regime each of the two terms corresponds to the HLN result of one of the two 2DEGs; each 2DEG contributes independently and additively to the magnetoconductivity. In the strongly coupled $\tau_c/\tau_\phi \ll 1$ regime the two terms σ_a, σ_b have two distinct values of L_ϕ which depend strongly on the both τ_c and τ_ϕ. The two L_ϕ's differ considerably. At small fields $L_B \gg L_c$ either σ_a or σ_b dominates the magnetoconductivity, similarly to a single 2DEG. Large enough fields disrupt the hopping between the 2DEGs and restore the magnetoconductivity to a sum of terms from two independent surfaces. Practically speaking, these results indicate that at small fields the magnetoconductivity can be fit well with an HLN curve with variable magnitude α. At strong coupling and weak fields one will find $\alpha = 1/2$, while at either weak coupling or strong fields $\alpha = 1$.

If we change the magnetic field's orientation to lie in-plane with the sample (and still perpendicular to the conduction), we obtain the problem of the in-plane magnetoconductivity. This signal must be absolutely null in a 2DEG with zero depth because there is no magnetic flux through the 2-D plane. Assuming that the electrons are free to diffuse throughout the vertical extent of the quantum well, Altshuler and Aronov published the first result which takes into account the 2DEG's depth.[23] They studied a dirty film where the scattering length l is much shorter than the sample thickness $L_y \gg l$ and obtained a logarithmic form:

$$\sigma_{AA} = -\alpha\frac{G_0}{2\pi}\ln|1+bB^2|,\ b = e^2L_y^2L_\phi^2/12\hbar^2 \quad (2)$$

Like the HLN result for perpendicular fields, the A-A formula for in-plane fields is quadratic at small fields and logarithmic at large fields, and displays a shoulder which transitions between the two. Unlike HLN, σ_{AA} depends on the sample thickness, is typically proportional to $L_\phi^2 \propto T^{-1}$ at small fields, and its shoulder occurs at a value of B which typically scales with $L_\phi^{-1/2} \propto T^{1/2}$. Later papers by Dugaev and Khmelnitsky and by Beenakker and Van Houten showed that these scaling laws are general to any model where charge moves

throughout the sample interior and the dephasing length L_ϕ is larger than the thickness.[24,25] Changing to a cleaner sample where $L_y \ll l$ only multiplies b by $3L_y/8l$, and changing the boundary conditions only multiplies b by a numerical constant.

It is straightforward to apply the A-A approach to calculate the effect of the surface state's penetration into the bulk, in a half-infinite TI. Tkachov and Hankiewicz reported that $b = 2e^2\lambda^2 L_\phi^2/\hbar^2$ where λ is the penetration depth.[26]

More interestingly, Raichev and Vasilopoulos (RV) calculated the in-plane magnetoconductivity of a pair of 2DEGs with random hopping.[27] This scenario is similar to a TI with no sides but with some random way for carriers to jump between the top and bottom surfaces. At strong coupling $\tau_\phi/\tau_c \gg 1$ RV obtain an A-A type formula with $b = e^2 L_y^2 L_\phi^2/4\hbar^2$, but at strong enough fields $bB^2 \geq \tau_\phi/\tau_c$ the in-plane magnetoconductivity saturates and becomes constant. At weak coupling $\tau_\phi/\tau_c \ll 1$ the magnetoconductivity is strongly suppressed, and in particular the quadratic coefficient b at small fields is multiplied by $\frac{4}{3}(\tau_\phi/\tau_c)^2$.

These results indicate that the coefficient b measured at small in-plane fields is sensitive to the intersurface hopping τ_c and to the temperature $\tau_\phi \propto 1/T$, and this has been confirmed experimentally.[30] They also indicate that b is three times bigger when current moves only on a TI's top and bottom surfaces than its value when current moves in the bulk; b can be used to measure the current distribution within a TI.[38] However these results give little insight into the physics to be expected from a TI's side surfaces, and no insight into topologically induced wrapping around the TI. In particular, is the coupling from side surfaces a strong coupling, or a weak coupling?

III. WEAK ANTILOCALIZATION OF A WRAPPED SURFACE STATE

The focus of our study is weak antilocalization, a quantum interference process which either adds to or subtracts from the probability that a charge will return to its starting point. One speaks of weak localization or weak antilocalization depending on the sign of the quantum correction to the return probability. On a TI surface the return probability is decreased, the conductivity increases, and this is called weak antilocalization. This is caused by the strong spin-orbit coupling found in TIs. In materials without a strong spin-orbit coupling one obtains the opposite effect, a decreasing conductivity called weak localization. The essential reason is that conduction is a long-distance phenomenon, and that the spin singlet channel and the three spin triplet channels contribute with opposite signs to the quantum interference diagrams. In materials with weak spin-orbit coupling both the spin singlet and the spin triplet persist over long distances, the three spin triplet channels win, and the net effect is an increased return probability. In contrast, it has been established both theoretically and experimentally that in TIs the spin relaxation length is very short.[14,31,36] Therefore only the spin singlet contributes to quantum interference, producing a decreased return probability and weak antilocalization.

The absence of long-distance spin physics also allows us to neglect the Zeeman energy, which ordinarily would mix the triplet channel with the singlet channel and thus destroy the weak antilocalization signal which is the focus of our article.[39] It is also known that Coulomb interactions combined with the Zeeman energy cause additional changes to weak antilocalization.[40,41] Fortunately both theory and experiment also verify that these effects disappear when the spin decay time is very short, as is the case on a TI surface.[14,31,40–42] In conclusion, the physics of weak antilocalization on the surface of a TI, because it concerns only long length scales, is entirely determined by diffusion of the spin singlet. In particular, spin triplet diffusion does not need to be modeled, and the effect of interactions on weak antilocalization can be neglected. At the long distance scales which concern us the only net effect of the TI's spin-orbit coupling are to destroy the spin polarization and reverse the overall sign of the quantum corrections. Therefore we will model only the singlet channel of quantum interference in a magnetic field.

In the diffusive regime, after many scatterings, the quantum correction to the conductivity at a position $\vec{x}$ is equal to:

$$\begin{aligned} \sigma_{WAL}(B,\vec{x}) &= G_0 \frac{D\tau}{\Gamma^0} \langle \vec{x}|\Gamma(B)|\vec{x}\rangle, \\ \Gamma(B) &= \Gamma^0(\tau/\tau_\phi - D\tau\,(\vec{\nabla} - \imath 2e\vec{A}/\hbar)^2)^{-1} \end{aligned} \quad (3)$$

where $\Gamma^0 = (2\pi\nu\tau)^{-1}$ describes the scattering strength and scatterer density, ν is the density of states, τ is the scattering time, and $\vec{A}$ is the gauge field associated with the magnetic field[52].[13,16,43,44]

The mathematical content of this formula is very simple - it simply calculates the return probability of a particle that starts at $\vec{x}$ and executes a random walk in a magnetic field $\vec{B} = \vec{\nabla} \times \vec{A}$. The result of many scatterings is diffusion, which is described by the diffusion kernel $D\tau\,(\vec{\nabla} - \imath 2e\vec{A}/\hbar)^2$. The additive constant τ/τ_ϕ describes gradual extinction of the random walker at the dephasing time scale τ_ϕ, and the matrix element $\langle \vec{x}|\Gamma(B)|\vec{x}\rangle$ extracts the random walker's return probability. A last detail is left implicit in our formula: an ultraviolet cutoff at the scattering length l. We are concerned with random walks with an average step length l, so we exclude length scales smaller than l and energy scales higher than $E_l = L_\phi^2/l^2$.

The only tricky issue here is the identity of the random walker. It is not electronic charge, as can be seen from the factor of $2e$ - not e - which multiplies the gauge potential. Instead it is the Cooperon, a disorder-induced correlation between the electron wave-function ψ and its complex conjugate $\psi^\dagger$, which is completely responsible for both weak localization and weak antilocalization. The correlation in question here is of a very special nature:

the Cooperon describes correlations where on one hand ψ executes random walks, while on the other hand $\psi^\dagger$ executes time-reversed copies of the same random walks. For this reason the Cooperon can not be reduced to classical physics; it is a distinctly quantum phenomenon. For the same reason the Cooperon is extremely sensitive to anything which breaks time reversal symmetry, which is why weak antilocalization has such a distinctive signal at small magnetic fields.

$\sigma_{WAL}(B,\vec{x})$ is an inherently position-sensitive quantity, describing the quantum probability of returning to point $\vec{x}$. It is sensitive to the device geometry and also to spatial variations in the diffusion constant, dephasing time, and magnetic field. In previous works on quantum wells such spatial dependence has been neglected because the quantum well's geometry is well approximated by an infinite plane with translational invariance. Here we consider TIs, where the conduction occurs on a surface which always completely wraps the TI bulk. Therefore we must track explicitly spatial variations in $\sigma_{WAL}(B,\vec{x})$. The dominant source of these variations is changes in the amount of magnetic flux piercing the surface. We will neglect subleading effects, such as the sensitivity of the surface state dispersion to the crystallographic orientation of the TI surface.[45,46] Variations in the diffusion constant and dephasing time, whether within the TI's surfaces or when crossing the edges between surfaces, are outside the scope of this article, and we will fix these constants to spatially uniform values.

The experimental observable that has been measured widely is not the local conductivity $\sigma_{WAL}(B,\vec{x})$, but instead the global conductivity $\sigma = GL/W$ of the TI device. In the diffusive regime where electrons diffuse freely around the TI surface, the global conductivity is equal to the spatial average of $\sigma_{WAL}(B,\vec{x})$, which will be our focus:

$$\begin{aligned}\langle\sigma_{WAL}(B)\rangle &= G_0 L_\phi^2 \int \frac{d^2\vec{x}}{L_r L_z}\,\langle\vec{x}|\tilde{\Gamma}(B)|\vec{x}\rangle,\\ \tilde{\Gamma}(B) &= (-L_\phi^2(\vec{\nabla}-\imath 2e\vec{A}/\hbar)^2+1)^{-1} \qquad (4)\end{aligned}$$

The $d^2\vec{x}$ integral covers the entire surface of the TI sample. L_r is the sample's perimeter and L_z is its length, so $L_r L_z$ is the surface area.

We note immediately that because Cooperon kernel is diffusive, and because a decay term equal to 1 is added to $-L_\phi^2\vec{\nabla}^2$, the Cooperon decays exponentially at the dephasing length L_ϕ. Therefore weak antilocalization is not sensitive to the TI surface's wrapping around the sample, unless the perimeter L_r is either comparable to or smaller than L_ϕ. This same condition regulates the existence of Altshuler-Aronov-Spivak (AAS) oscillations, another weak antilocalization signal which occurs when the magnetic field is oriented longitudinally with the axis of conduction.

A. Reduction to a One Dimensional Problem

In a magnetic field a charged particle executes circular motion around a slowly moving point called the guiding center that drifts in response to external forces. In our problem there are no forces other than the magnetic force, so the guiding center's momentum is conserved. We take advantage of this and choose a gauge potential which preserves translational invariance along the $\hat{z}$ axis of conduction. This technique effectively solves the guiding center's motion. We choose a gauge potential $\vec{A} = A_z\hat{z}$ that is aligned with the $\hat{z}$ axis. We restrict it to depend only on r, the coordinate which wraps around the TI surface. These choices simplify the Laplacian to $(\vec{\nabla}-\imath 2e\vec{A}/\hbar)^2 = -(k_z - 2eA_z(r)/\hbar)^2 + (\partial/\partial_r)^2$. We have preserved translational invariance along the $\hat{z}$ axis and therefore can resolve the Cooperon with the z momentum k_z. A simple exercise obtains the equations which we will use for our numerical calculations:

$$\begin{aligned}\langle\sigma_{WAL}(B)\rangle &= \frac{G_0}{4\pi}\,x\int\frac{dR_g}{L_r}\int dr\\ &\quad \langle r|(V(r,R_g)-L_\phi^2(\partial/\partial_r)^2+1)^{-1}|r\rangle,\\ &= \frac{G_0}{4\pi}\,x\int\frac{dR_g}{L_r}\,Tr(\,A^{-1}\,)\\ &= \frac{G_0}{4\pi}\,x\int\frac{dR_g}{L_r}\sum_i^{E_i<E_l} E_i^{-1},\ E_i|i\rangle = A|i\rangle\\ A = &\quad V(r,R_g)-L_\phi^2(\partial/\partial_r)^2+1,\\ V(r,R_g) &= (x^2/4L_\phi^2)(R(r)-R_g)^2\\ R(r) &= -2eA_z(r)L_B^2/\hbar,\ R_g = -L_B^2 k_z \qquad (5)\end{aligned}$$

Here and elsewhere $x = 2L_\phi^2/L_B^2$ is a dimensionless variable that is proportional to the magnetic field strength B. We now have an integral over the guiding center's longitudinal momentum k_z, which is linearly related to $R_g = -L_B^2 k_z$, the guiding center's equilibrium position on the r coordinate which parameterizes the TI's perimeter. For each particular value of $R_g \propto k_z$ we must solve a 1-D Schrodinger equation $E_i|i\rangle = A|i\rangle = (V(r,R_g) - L_\phi^2(\partial/\partial_r)^2+1)|i\rangle$ describing the problem of cyclotron motion in the TI's magnetic field.

In the limit of an infinitely wide 2-D surface with no boundaries or sidewalls, the potential $V(r,R_g)$ in equation 5 is quadratic, and the eigenvalue problem $E_i|i\rangle = A|i\rangle$ maps exactly to the Landau level problem. The energies are $E_i = (i+1/2)\omega_C + 1$ where $\omega_C = 2L_\phi^2/L_B^2 = x$ is the cyclotron frequency of the Cooperon. Equation 5's sum over the equally spaced Landau level energies E_i can be summed analytically, producing the HLN formula found in equation 1.

In a TI with top and bottom surfaces and sidewalls the potential $V(r,R_g)$ is not a simple quadratic, which will force us to use numerical not analytical methods to evaluation equation 5. If the TI sample's height and width are L_y, L_x respectively and the magnetic field is aligned

at an angle θ with respect to the y axis which lies normal to the TI's top and bottom surfaces, then the $R(r)$ function figuring in the potential is:

$$R(r) = \begin{cases} (r - L_x/2)\cos\theta - (L_y/2)\sin\theta, & 0 < r < L_x \\ (L_x/2)\cos\theta + (r - L_x - L_y/2)\sin\theta, & L_x < r < L_x + L_y \\ (-r + 3L_x/2 + L_y)\cos\theta + (L_y/2)\sin\theta, & L_x + L_y < r < 2L_x + L_y \\ -(L_x/2)\cos\theta + (-r + 2L_x + 3L_y/2)\sin\theta, & 2L_x + L_y < r < 2L_x + 2L_y \end{cases}$$

The second moment of $R(r)$ is:

$$\langle R^2(r)\rangle = \frac{(L_x/3 + L_y)L_x^2\cos^2\theta + (L_x + L_y/3)L_y^2\sin^2\theta}{4(L_x + L_y)} \tag{6}$$

On each surface we have a quadratic potential $V(r, R_g) = (x^2/4L_\phi^2)(R(r) - R_g)^2$ with minima located at R_g. This potential describes the fact that eigenstates are constrained to orbit R_g. A state with energy E has cyclotron radius $(2L_\phi/x)\sqrt{E}$, and decays exponentially outside that radius. The largest permitted cyclotron radius is determined by the ultraviolet cutoff $E_l = L_\phi^2/l^2$, is equal to $\delta R = L_B^2/l = 2L_\phi^2/lx$, and scales with B^{-1}.

Since $R(r)$'s range is limited to the interval $[-(L_x|\cos\theta| + L_y|\sin\theta|)/2, +(L_x|\cos\theta| + L_y|\sin\theta|)/2]$, we can set R_g's limits of integration at $\pm((L_x|\cos\theta| + L_y|\sin\theta|)/2 + \delta R)$.

B. Classification of Cooperon Eigenstates

Equation 5's structure, which is centered on a Schrodinger equation $E_i|i\rangle = A|i\rangle$ with a non-uniform potential, indicates that the eigenstates $|i\rangle$ are crucial to determining the magnetoconductivity. These are not electron states. They are eigenstates of the Cooperon operator, the diffusive operator which controls the interference diagrams that cause weak antilocalization. We can immediately distinguish four types of Cooperon eigenstates by comparing their eigenvalues E_i to the maximum value of the potential, which is $V_{max}(k_z) = L_\phi^2((L_x/2L_B^2)|\cos\theta| + (L_y/2L_B^2)|\sin\theta| + |k_z|)^2$. The four types of states are:

1. **Wrapped States.** If the energy E_i is large enough that it exceeds V_{max}, then the state wraps around the entire TI nanowire.

2. **Harmonic Oscillator states.** If the energy E_i is smaller than V_{max}, AND if $E = E_i$ intersects the potential at two points on *the same face* of the TI, then the state is trapped on that face and executes cyclotron motion there.

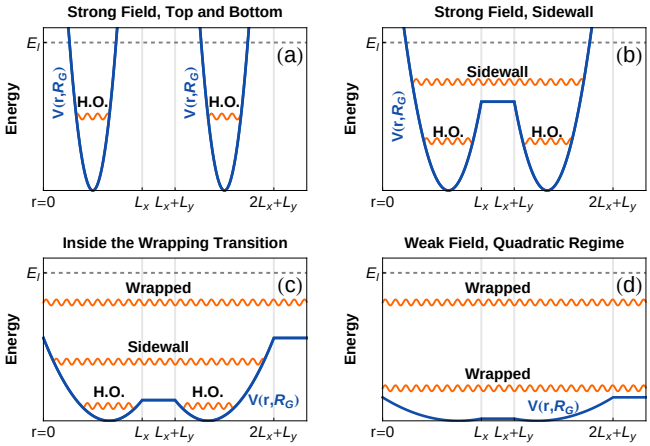

FIG. 2: (Color online.) The potential and the Cooperon eigenstates. The grey dashed lines sketch the potential $V(r, R_g)$ as a function of the coordinate r which wraps around the TI sample. $E_l = L_\phi^2/l^2$ represents the ultraviolet cutoff. The orange wavy lines illustrate typical harmonic oscillator, sidewall, and wrapped states. Pane (a) illustrates a strong magnetic field with $R_g = L_x/2$ positioned in the middle of the top face; all states are harmonic oscillator (H.O.) states centered at R_g. Pane (b) illustrates a strong magnetic field with $R_g = 0.8L_x$ near the sidewall, allowing some sidewall states. Pane (c) illustrates a weaker field inside the wrapping transition, allowing wrapped states. Pane (d) illustrates a very weak field where all states wrap the TI.

3. **Sidewall states.** If the energy is smaller than V_{max}, AND if $E = E_i$ intersects the potential on *two opposite faces* of the TI (for example the top and bottom), then the state is spread across three faces of the TI. We focus on the particular case where the magnetic field B is perpendicular to the TI top surface; in this case the state moves as a plane wave on one of the TI's sidewalls and penetrates only a small distance into the top and bottom faces, where it executes cyclotron motion. We call this a sidewall state.

4. **Edge states.** If the energy is smaller than V_{max}, AND if $E = E_i$ intersects the potential on *two adjacent faces* of the TI, then the state is trapped

at the corner between those two faces; it is an edge state. This type of state occurs only when the magnetic field is at an angle relative to perpendicular, i.e. when $\theta \neq 0$.

C. Numerical Implementation

All of our numerical results in the next section were obtained by numerically evaluating equation 5. Our numerical implementation is straightforward. We evaluate $-L_\phi^2(\partial/\partial_r)^2$ by discretizing on a lattice in position space with lattice spacing a; we obtain $-L_\phi^2(\partial/\partial_r)^2 = 4L_\phi^2 \sin^2(k_r a/2)/a^2$. We choose $a = l\sqrt{2}$, so the maximum value of the kinetic term is $2E_l$. The finite lattice spacing does introduce certain numerical errors, but these have no physical significance because they just slightly redefine the high-momentum cutoff at $E_l = L_\phi^2/l^2$.

To obtain a numerically efficient calculation we cap the potential at $2E_l$, so that the spectrum is bounded above at about $4E_l$. For safety we take the upper bound as $4.1\ E_l$.

Numerically we implement the ultraviolet $E_l = L_\phi^2/l^2$ cutoff using this formula:

$$Tr(\ A^{-1}\ ) \ = \ Tr(\mathcal{D}/A),\ \mathcal{D} = \frac{1}{2}(1 - \tanh((A - E_l)/\delta))$$

The operator $\mathcal{D}$ is just a smoothed step function. δ sets the width of the energy cutoff, which is centered around $E_l = L_\phi^2/l^2$. The tanh function inside of $\mathcal{D}$ is approximated by a Chebyshev polynomial, and we choose δ to match the polynomial's order K; $\delta \approx 4E_l/K$. We have checked that all of our results have converged with respect to K.

We discretize the R_g integral on a grid with $2N_z + 1$ points and check for convergence with respect to N_z. Generally speaking, convergence occurs very quickly once N_z reaches a threshold value that is proportional to the sample perimeter L_r.

D. Important length scales and parameters

Our model has the following parameters:

- $L_\phi = \sqrt{D\tau_\phi}$, the dephasing length which regulates the Cooperon decay. This is the length that a particle can diffuse before dephasing occurs. In diffusive 2-D systems τ_ϕ scales inversely with temperature T, so $L_\phi \propto T^{-1/2}$.
- L_x, L_y, and $L_r = 2L_x + 2L_y$, the sample width, height, and perimeter. We will show that when these scales are long compared to L_ϕ the HLN result is, at leading order, simply reduced by a factor of $2L_x/L_r$.
- l, the scattering length, which determines the Cooperon's ultraviolet cutoff $E_l = L_\phi^2/l^2$.
- θ, the angle of the magnetic field.
- B, the magnetic field strength. Instead of B we will usually discuss the dimensionless variable $x = 2L_\phi^2/L_B^2 = 4eL_\phi^2 B/\hbar$, which is proportional to B. Our model gives spurious results when B is strong enough that cyclotron radius is near the scattering length. Practically speaking, this occurs when $x/E_l = 2l^2/L_B^2 > [0.3, 1]$.
- $\delta R = L_B^2/l = 2L_\phi^2/lx$, the cyclotron radius of the highest Landau levels at energies near the ultraviolet cutoff E_l.

IV. RESULTS

A. The geometric factor at large B.

A TI sample's sidewalls are not pierced by a magnetic flux when the magnetic field is perpendicular to the sample's top and bottom faces. Therefore quantum interference diagrams occurring only on the sidewalls are completely unaffected by the magnetic field. This reduces the sample's average magnetoconductivity, as compared to a simple TI model without sidewalls.

The magnetoconductivity including sidewalls is, in the most general case, difficult to compute because some interference diagrams visit both the sidewalls and the sample top and bottom, and this computation is the main focus of this paper. However a simpler case exists which is relevant to most TI weak antilocalization experiments, where the decoherence length L_ϕ is small compared to the sample height L_y and width L_x. In these experiments only a small fraction of the quantum interference involves two or more of the sample's faces, and the following result is easily derived:

$$\langle \sigma_{WAL}(B) \rangle \ = \ \frac{2L_x}{L_r}\sigma_{HLN}(x) + O(L_\phi/L_x) + O(L_\phi/L_y) \tag{7}$$

$\sigma_{HLN}(x)$ is the HLN conductivity of two separate TI surfaces. The point is simple: the HLN conductivity is multiplied by a factor of $2L_x/L_r < 1$. Figure 3 confirms this result by plotting the magnetoconductivity in samples of fixed width $L_x = 10$, as the sample height L_y is varied from 30 to 0. The magnetic field strength is kept fixed at four values $L_B^2 = [1.25, 2.5, 5, 10]$, the dephasing length is $L_\phi = 5$, and the scattering length is $l = 0.5$. When the sample is of height $L_y = 30$ we expect to obtain $0.25\ \sigma_{HLN}(x)$, while in an infinitely thin sample we expect the unmodified HLN result, and we expect a linear dependence on $2L_x/L_r$ in intermediate cases.

Figure 3 shows our numerical results, which were obtained by evaluating equation 5. They confirm Eq. 7

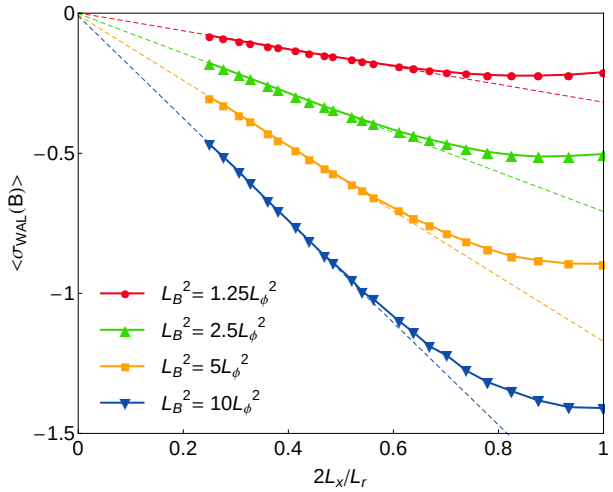

FIG. 3: (Color online.) The TI average magnetoconductivity $\langle\sigma_{WAL}(B)\rangle$ is reduced by the TI sidewalls. The solid lines plot $\langle\sigma_{WAL}(B)\rangle$ as a function $2L_x/L_r$, where L_x is the sample width and L_r is the sample perimeter. The four lines, from top to bottom, hold the magnetic field fixed at $L_B^2 = [1.25, 2.5, 5, 10]\, L_\phi^2$. The coherence length is much smaller than the sample perimeter. The dashed lines are linear fits to the data, and their excellent agreement with the data at $2L_x/L_r < 0.5$ demonstrates that sidewalls multiply the HLN conductivity by $2L_x/L_r$. The deviation from linearity in thin samples shows that even in infinitely thin samples the conductivity is less than the HLN prediction because the top and bottom are coupled at the TI's sides.

when $2L_x/L_r < 0.5$; i.e. when the sample thickness L_y is large enough to exceed two decoherence lengths $L_y > 2L_\phi$. In thinner samples with $L_y < 2L_\phi$ Figure 3 reveals that our linear formula overestimates the magnetoconductivity. In other words, even in infinitely thin samples with no sidewalls the magnetoconductivity is always less than the HLN result. We expect this undershoot in the thin limit to be proportional to L_ϕ/L_x.

These results apply only when L_ϕ is small compared to the sample size. We also have studied smaller samples, and confirmed that the linear scaling disappears.

In conclusion, at small L_ϕ a TI with sidewalls will never attain the HLN prediction. In thin samples the real conductivity will reduced by a term of order L_ϕ/L_x, while in thicker samples the HLN result will be multiplied $2L_x/L_r$. This result will be of considerable interest to WAL experiments where the magnetoconductivity's magnitude has been used to count the number of independent conducting 2-D channels and to analyze the coupling strength between a TI's top and bottom surfaces.

B. The Regime of Wrapped Cooperon States

We now turn toward systems whose perimeter L_r is comparable to or smaller than the dephasing length L_ϕ, bringing weak antilocalization into a regime that is sensitive to each of the TI's faces. Figure 4a shows our results for the magnetoconductivity $\langle\sigma_{WAL}(x)\rangle$ as a function of the dimensionless parameter x, which is proportional to B. Here we treat the simple case of thin samples with height $L_y = 0$, and we will discuss thicker samples later. The scattering length is $l = L_\phi/100$. The black line on the left of Figure 4a is the HLN curve, which is realized in samples with width L_x far exceeding L_ϕ. Moving to the right, the solid curves with symbols show successively samples with widths $L_x = [0.8, 0.4, 0.2, 0.1]\, L_\phi$. The main qualitative features are immediately clear: in finite samples the sensitivity to magnetic field is reduced, and the HLN curve's shoulder at $x \approx 1$ is replaced by a structure that moves steadily to higher magnetic fields as the sample size decreases. Attempts to fit this magnetoconductivity to the HLN curve will obtain a value of L_ϕ which is reduced by a large multiplicative factor controlled by the sample width L_x. The fitted value of L_ϕ will be proportional to L_x, not to the much larger value of L_ϕ.

Key to these results is the radius of cyclotron orbits, because this length scale limits exploration of the TI perimeter. The cyclotron radius is larger for higher excited states, and is $\delta R = L_B^2/l$ at the ultraviolet cutoff $E_l = L_\phi^2/l^2$. At high fields δR becomes so small that states are unable to cross between faces, and we obtain the modified HLN formula $\frac{2L_x}{L_r}\sigma_{HLN}(x)$, which is proportional to $\ln x$. Therefore at high fields we always obtain the HLN logarithm. This is confirmed by the high-field sector (right side) of Figure 4a. In this semilog plot all five curves are linear at large B, matching nicely the straight lines. This linear behavior on our semilog plot shows that the conductivity increases logarithmically with the system size, exactly as predicted by the HLN formula.

The HLN logarithm terminates at small fields where $L_B \propto L_\phi$, $x \propto 1$, and transitions into quadratic behavior. Figure 4a shows that a TI sample begins to deviate from HLN logarithmic behavior at far larger field strengths. The deviation begins with a wrapping transition, where the cyclotron radius becomes large enough to allow states to completely wrap the TI sample. Comparison of the magnetic potential $V(r, R_g)$ with the ultraviolet cutoff at $E_l = L_\phi^2/l^2$ indicates that the highest energy states start to wrap the sample when $L_x|\cos\theta| + L_y|\sin\theta| = 2\delta R$, which in a perpendicular field simplifies to $L_B^2 = L_x l/2$. This is confirmed by our numerical results shown in Figure 4a. The wrapping formula predicts that the wrapping transition is at $x = [500, 1000, 2000, 4000]$ for the $W = [0.8, 0.4, 0.2, 0.1]\, L_\phi$ samples. For the rightmost line ($W = 0.1\, L_\phi$) the predicted transition value $x = 4000$ puts L_B too close to the scattering length l to obtain good accuracy, and the wrapping transition is hard to pin down. However the three other lines at $W = [0.8, 0.4, 0.2]\, L_\phi$ show clear wrapping transitions. The arrows highlight the points where the numerical data show clear wrapping transitions, and these points agree very well with our wrapping formula, $L_B^2 = L_x l/2$.

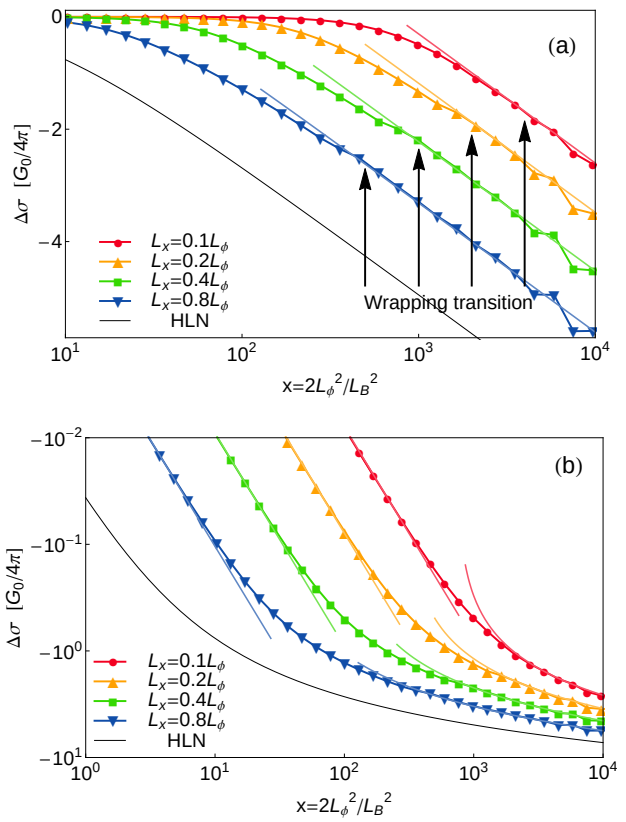

FIG. 4: (Color online.) The Wrapping Transition. Pane (a) shows the magnetoconductivity $\langle \sigma_{WAL}(B) \rangle$ as a function of $x \propto B \propto L_B^{-2}$. The four lines are for four sample widths, from left to right $L_x = [0.8, 0.4, 0.2, 0.1]\, L_\phi$. The HLN curve is plotted in black. At high fields the data matches logarithms similar to the HLN curve, seen as straight lines on this semilog plot. At $x = 4L_\phi^2/L_x l$ the data departs from a logarithm because Cooperon eigenstates begin to wrap around the TI sample, becoming sensitive to its topology. Pane (b) shows the same data on a log-log plot. The small-field data matches well to quadratic curves, seen here as straight lines, and is controlled entirely by wrapped states. The small-field regime ends at $L_B^2 < L_x^2/2$, when the potential becomes strong enough to cause bound states.

It is an amazing fact that the wrapping transition is controlled by two very disparate length scales: the scattering length l, and the system width L_x.[53] This is a consequence of the equipartition of energy between kinetic and potential energy. In the Landau level problem the potential energy is $L_\phi^2 \langle r^2 \rangle / 2L_B^4$ and the kinetic energy is $L_\phi^2 \langle k^2 \rangle / 2$, where k is the wave-number and r is the radius. Setting the two equal, we obtain $\langle k^2 \rangle = \langle r^2 \rangle / L_B^4$. This evidences the linear relation between a state's momentum and radius, which is a special feature of the Landau level problem. In other words, states with large spatial extension also have large momenta; their spatial oscillations are faster. This is why the wrapping transition is sensitive to the scattering length. A change in scattering length translates directly to a corresponding change in the state's maximum spatial extent, which never exceeds L_B^2/l. Comparing the state's extent to $L_x/2$, we recover the equation for the wrapping transition, $L_B^2 = L_x l/2$.

The wrapping transition can be observed only if it occurs at a field strength which significantly exceeds the HLN shoulder at $L_B = L_\phi$; i.e. if $L_x l/2 < L_\phi^2$. Using $L_\phi^2 = D\tau_\phi = l v_F \tau_\phi/2$, this condition simplifies to $L_x < v_F \tau_\phi$, where v_F is the Fermi velocity. In other words, the wrapping transition occurs only when the width L_x is smaller than $v_F \tau_\phi$, the length that the electron can move ballistically before dephasing. This formula is very remarkable, for it reveals a ballistic scale deep in the diffusive regime.

C. Inside the Wrapping Transition

Figure 4b focuses on the region inside the wrapping transition. It shows the same data as Figure 4a, but in a log-log format which accentuates small values of the magnetoconductivity and reveals a straight line when the signal follows a power law. We can distinguish two regimes inside the wrapping transition. First we discuss small fields, where we have plotted quadratic curves as straight lines without symbols. The quadratic lines coincide very nicely with the signal, which is always quadratic at small magnetic field. The range of quadratic behavior is *very roughly* $x < 4L_\phi^2/L_x^2$, which corresponds to values of the magnetic length L_B^2 exceeding $L_x^2/2$. In this regime the magnetic field is not strong enough to create Cooperon bound states, and all Cooperon states wrap around the sample. The observed quadratic signal is similar to the HLN formula's quadratic regime where $\langle \Delta\sigma_{WAL}(x) \rangle = x^2/24$ when L_B exceeds L_ϕ, but here the signal is much weaker and extends to much larger field strengths.

Simple dimensional analysis shows that in the quadratic region where $\Delta\sigma_{WAL}(x)\rangle \propto B^2 \propto L_B^{-4}$, the magnetoconductivity must contain some length scale to the fourth power, to compensate for $B^2 \propto L_B^{-4}$. In the HLN formula we have L_ϕ^4/L_B^4, while the in-plane magnetoconductivity is proportional to $L_y^2 L_\phi^2/L_B^4$. Our data in Figure 4b completely excludes either type of scaling in the wrapped regime. HLN scaling would produce an extra feature at $x = 1$, while scaling with $L_x^2 L_\phi^2/L_B^4$ would produce features at values of $x = [2.5, 5, 10, 20]$. Both types of scaling are absent. Moreover, our analysis of the weak field data in Figure 4b at four values of the sample width L_x indicates that the conductivity here is scaling with $L_x^{3.5}$, and suggests that the conductivity scales as $\Delta\sigma_{WAL}(x)\rangle \propto L_x^{3.5} L_\phi^{0.5} L_B^{-4}$. We conclude that the conductivity's dependence on L_ϕ is strongly suppressed, and we will discuss this further in the next section.

In addition to the quadratic regime governed by wrapped states, Figure 4b shows also an intermediate regime lying between the quadratic region at $L_B^2 \approx L_x^2/2$

and the wrapping transition at $L_B^2 = L_x l/2$. Here the low energy Cooperon states do not make a full circuit around the TI, and remain restricted to one, two, or three faces. Therefore the signal includes contributions not only from wrapped states, but also from the harmonic oscillator, sidewall, and (in tilted fields) edge states which we have discussed earlier. We analyze the harmonic oscillator and wrapped contributions in Appendix A. Since this intermediate regime interpolates between the quadratic signal seen at weak fields and the HLN logarithm at strong fields, in this regime the magnetoconductivity will look roughly linear.

D. Suppression of Sensitivity to L_ϕ and to Temperature Inside the Wrapping Transition

The HLN formula is based on the assumption that the Cooperon is able to travel a distance L_ϕ, where L_ϕ is associated with quantum decoherence and typically scales with $L_\phi \propto T^{-1/2}$ in 2-D diffusive systems. In this article we concern ourselves with wires that are smaller than L_ϕ, so that states are able to wrap around the wire's perimeter. In this scenario the perimeter L_r provides the fundamental upper limit on the Cooperon's travel distance, and its dependence on L_ϕ and on T are suppressed.

Mathematically, the mechanism by which the L_ϕ dependence is suppressed in small samples originates with the level spacing of the eigenvalues of the Cooperon diffusion operator. At $B = 0$ the energy levels are $L_\phi^2 k_r^2 = n_r^2 (2\pi L_\phi / L_r)^2$, with a level spacing of order $(2\pi L_\phi/L_r)^2$. This quantity should be added to the 1 in the diffusion operator. Therefore we adopt the following prescription for small samples: we replace L_ϕ^2 with a new length scale $L_{\phi r}^2$, given by $L_{\phi r}^{-2} = L_\phi^{-2} + (L_r/2\pi)^{-2}$. This change of course does not affect the ultraviolet cutoff, which remains $E_l = L_\phi^2/l^2$. The net effect is that in small samples L_ϕ should be replaced by $L_r/2\pi$ which is independent of temperature, and in larger samples we use $L_{\phi r}$ which retains some weakened temperature dependence.

In appendix A 1 we perform an analytical analysis of the quadratic regime, which is governed by wrapped Cooperon states. We find that in this regime the conductivity is governed by two dimensionless constants. The first constant γ is determined by semiclassical considerations and is equal to $\gamma = \langle R^2(r)\rangle\, L_{\phi r}^2/L_B^4$, where $\langle R^2(r)\rangle$ is the second moment of $R(r)$ and is given in equation 6. γ scales with temperature as $\gamma \propto L_{\phi r}^2$; it is independent of temperature in small samples and scales with $1/T$ in large samples. The second dimensionless constant is λ^4/L_B^4, where $\lambda \le L_r$ is an explicitly quantum quantity that is independent of both $L_{\phi r}$ and temperature T. λ^4/L_B^4 difficult to compute analytically. It is never significantly greater than γ, and may be considerably smaller than γ.

If we omit λ^4/L_B^4 from our considerations, we obtain

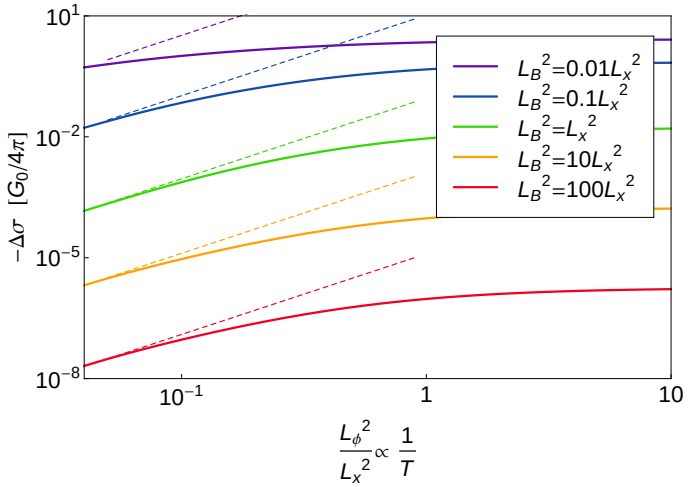

FIG. 5: (Color online.) Suppression of sensitivity to the dephasing length L_ϕ and the temperature T. We plot the magnetoconductivity $\langle \sigma_{WAL}\rangle$ as a function of L_ϕ^2, the square of the dephasing length, which is inversely proportional to the temperature T. We keep the magnetic field strength fixed at five values $L_B^2 = [0.01, 0.1, 1, 10, 100]\, L_x^2$. On this logarithmic graph the dashed lines show the scaling predicted by the HLN formula, $\sigma \propto L_\phi^4 \propto 1/T^2$, and match the conductivity when the coherence length is small $L_\phi \ll L_x$ and the magnetic field is also small. When the coherence length is large (on the right side of the graph) the HLN formula fails and σ is independent of both L_ϕ and T.

equation A3 for the magnetoconductivity, which we repeat here:

$$\langle \Delta\sigma_{WAL}(B)\rangle \;=\; -\frac{G_0}{4\pi}\ln|1+\gamma|,\ \gamma = \frac{L_{\phi r}^2\langle R^2(r)\rangle}{L_B^4} \quad (8)$$

This allows us to reach some conclusions about the quadratic coefficient b which controls the conductivity at small fields via $\langle \Delta\sigma_{WAL}(B)\rangle = -(G_0/4\pi)\, bB^2$. The HLN formula, which applies in large samples with large magnetic fields outside the wrapping transition, gives $b = 2e^2 L_\phi^4/3\hbar^2 \propto 1/T^2$. In contrast, inside the wrapping transition we find that

$$b \;\propto\; \frac{4e^2}{\hbar^2}\langle R^2(r)\rangle\, L_{\phi r}^2 \quad (9)$$

This b scales with $L_r^2 L_\phi^2 \propto 1/T$ in samples that are much larger than L_ϕ. As L_ϕ is increased and surpasses the sample dimensions, the dependence on L_ϕ and temperature T are suppressed, and σ becomes completely independent of these quantities. It scales instead with the sample dimension - $b \propto L_r^4$ - in samples that are small compared to L_ϕ. Figure 5 illustrates this effect at five values of the magnetic field strength corresponding to cyclotron radii L_B which are smaller than, equal to, and greater than the sample size L_x. The lower curves in Figure 5 show weak fields, i.e. $L_B \gg L_x$, where the magnetoconductivity is quadratic in B. Along the x axis we vary the ratio

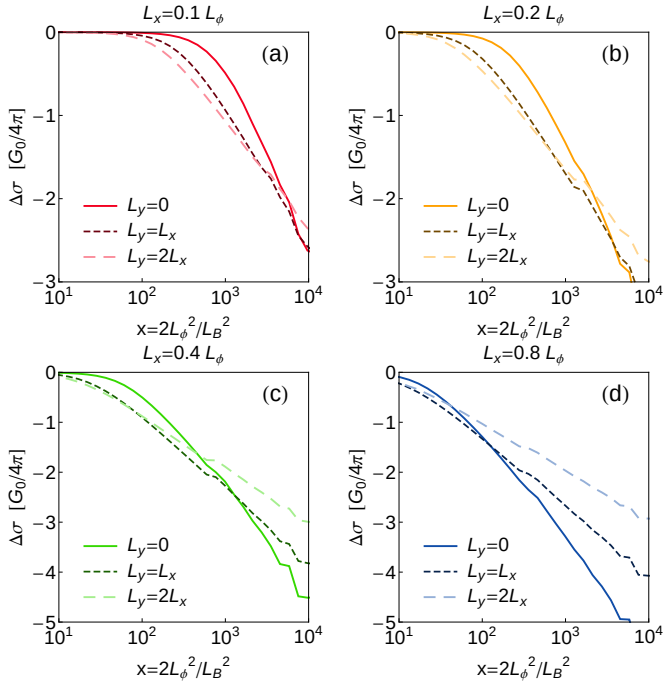

FIG. 6: (Color online.) The effect of sample height. We plot the magnetoconductivity $\langle\sigma_{WAL}(x)\rangle$ as a function of $x \propto B$ at three aspect ratios $L_y = [0, L_x, 2L_x]$, signaled by unbroken lines, short dashes, and long dashes respectively. We show samples with width $L_x = [0.8, 0.4, 0.2, 0.1]\, L_\phi$. Inside the wrapping transition $\langle\sigma_{WAL}(x)\rangle$ increases when L_x increases, while the trend is reversed at large fields.

of L_ϕ to the sample size. On the left side of Figure 5 L_ϕ is small and our numerical results match well to the HLN $\sigma \propto L_\phi^4 \propto 1/T^2$ curves. As L_ϕ is increased our numerical curves progressively depart from the HLN prediction. At $L_\phi \geq L_x$ the conductivity is roughly constant with respect to L_ϕ; the temperature dependence is completely suppressed.

This effect will be easy to measure experimentally by reducing the temperature while keeping the magnetic field constant. It will manifest itself as a plateau in the magnetoconductivity at low temperatures where the dephasing length becomes comparable to the sample size.

E. Changes in the sample height L_y.

Our previous results concerned infinitely thin TI samples. This geometry is a good approximation to thin films, which often have a width of microns and a depth of tens of nanometers. Here we examine the magnetoconductivity of thicker samples. The unbroken lines in Figure 6 show the zero-thickness results presented earlier, the lines with short dashes show square samples with height equal to width $L_y = L_x$, and the lines with long dashes show samples where the height is twice the width $L_y = 2L_x$.

Outside of the wrapping transition, at large fields, increasing the sample height causes the magnetoconductivity to decrease. This is caused by the $2L_x/L_r$ multiplier which we have discussed earlier. While this multiplier is not accurate in small samples where $L_r \ll L_\phi$, it does become important when the sample height is increased, because the perimeter grows with sample height and eventually exceeds the dephasing length.

Inside the wrapping transition, at small fields, the trend reverses; increasing the sample height causes $\langle\sigma_{WAL}(B)\rangle$ to increase. Consistently with this, the wrapping transition moves to smaller field strengths. This is an interesting signal of the TI's topology - if there were no transport along the sidewalls then the dependence on L_y would be precisely null.

Quantitatively, the weak-field conductivity of an $L_x \times L_y = 0.1L_\phi \times 0.1L_\phi$ sample is a factor of 5.5 larger than that of an $L_x \times L_y = 0.1L_\phi \times 0$ sample. When the height is doubled to $L_y = 0.2L_\phi$, the conductivity is multiplied by an additional factor of 2.3. This $L_x \times L_y = 0.1L_\phi \times 0.2L_\phi$ conductivity actually exceeds that of a wider but thinner $L_x \times L_y = 0.2L_\phi \times 0$ sample.

This effect and its sign can be understood analytically in terms of the coefficient b which controls the conductivity at small fields, which we reported earlier:

$$b \;\propto\; \frac{4e^2}{\hbar^2}\langle R^2(r)\rangle\, L_{\phi r}^2 \qquad (10)$$

If the coherence length is much larger than the sample size $L_r/L_\phi \ll 1$, then $L_{\phi r} \approx L_r$, which doubles when the height is increased from zero to $L_y = L_x$. The second moment $\langle R^2(r)\rangle$ is also doubled (see equation 6), so b's net increase is a factor of 8. An additional height doubling to $L_y = 2L_x$ causes b to multiply by an additional factor of 2.625. Our numerical results are a bit less than these analytical predictions because we are not precisely in the $L_r/L_\phi \ll 1$ limit; instead we have $L_r/L_\phi = [0.2,\ 0.4,\ 0.6]$.

F. Tilted Magnetic Fields

Several experiments have reported tilted field measurements to confirm that in thin samples the observed magnetoconductivity is sensitive only to the perpendicular component of the magnetic field, $B\cos\theta$. Using $B\cos\theta$ as the x-axis and $\Delta\sigma$ as the y axis, these experiments showed agreement between measurements performed at different angles.[14,28,29,31–35] However many find that the agreement fails at large angles or large fields, and many also observe also an in-plane ($\theta = \pi/2$) signal which is inconsistent with dependence only on a perpendicular field.[28,29,31,33,35] Here we present an analytical formula and numerical results on tilted fields.

A simple formula which takes into account both in-plane and perpendicular fields can be obtained when the dephasing length L_ϕ is short compared to the sample

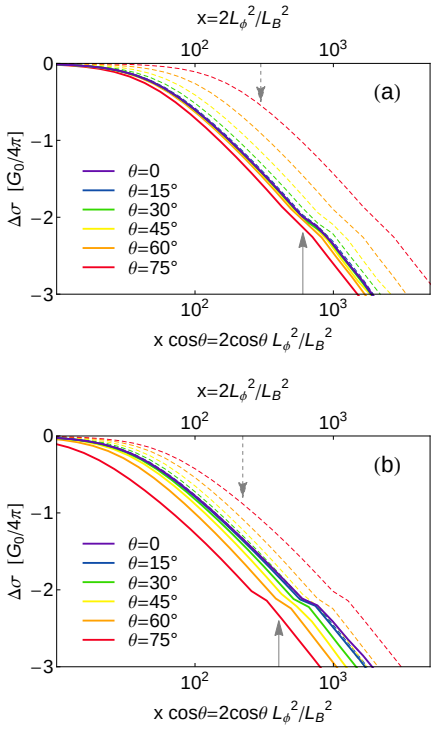

FIG. 7: (Color online.) Comparison between using the total magnetic field vs. its component perpendicular to the sample. We plot the magnetoconductivity $\langle\sigma_{WAL}(x)\rangle$ at six field angles between perpendicular $\theta = 0$ and $\theta = 75$ degrees. The unbroken lines are plotted with the perpendicular component $B\cos\theta$ as the x axis, while the dashed lines are plotted with the total field B as the x axis. In pane (a) we show a thin sample with $L_y = 0.1L_x$, where use of the perpendicular field $B\cos\theta$ causes a nice collapse of the lines on top of each other, showing that $\langle\sigma_{WAL}(x)\rangle$ substantially depends only on $B\cos\theta$. In pane (b) we show a thicker sample with $L_y = 0.4L_x$, and find that the $B\cos\theta$ plot has no advantage over the B plot.

size L_r. In this case the magnetoconductivity is a sum of separate contributions from the TI's faces:

$$\langle\sigma_{WAL}(B)\rangle \;=\; \frac{2L_x}{L_r}\sigma_{HLN}(x\cos\theta) + \frac{2L_y}{L_r}\sigma_{HLN}(x\sin\theta) \tag{11}$$

Corrections are of order $O(L_\phi/L_r)$. This same formula applies also to the regime of large magnetic fields, in which the cyclotron radius δR is much smaller than the sample size. This formula should be a distinct improvement over previous work which did not take into account the sidewall contribution $\frac{2L_y}{L_r}\sigma_{HLN}(x\sin\theta)$.

Figure 7 shows our numerical results for tilted field measurements. In pane 7a the width is $L_x = 0.4L_\phi$, the height is one tenth of the width, and the scattering length is $l = L_\phi/100$. We show results obtained at $\theta = 0, 15, 30, 45, 60$, and 75 degrees. To help the reader to make a comparison between plots using the perpendicular field $B\cos\theta$ and plots using the total field B, we plot both versions in the same graph. The unbroken lines are plotted using the perpendicular field $B\cos\theta$ as the x axis, while the dashed lines show same data but are plotted using the total field B as the x axis.

Figure 7a shows that in this thin $L_y = 0.1L_x$ sample the data agrees well with a perpendicular field dependence: the lines with squares lie very near to each other, with the furthest departure at 75 degrees. In particular, the agreement between perpendicular-field plots (unbroken lines) is a large improvement over the total-field plots (dashed lines), which proves that in this thin sample the perpendicular field, not the total field, controls the magnetoconductivity. It is remarkable that the agreement is this good even though wrapping effects are important. In fact the angular dependence shows no qualitative difference between small field strengths inside the wrapping transition and large field strengths outside the wrapping transition.

In contrast, in Figure 7b we show a thicker sample where $L_y = 0.4L_x$ and all other parameters remain the same. Here using a perpendicular field gives no improvement over using the total field as the x axis, presumably because the sidewall contribution is large. Again we see little qualitative difference between results inside and outside the wrapping transition.

Figure 8 shows our calculations of how the magnetoconductivity changes when the magnetic field angle is varied continuously between $\theta = 0$ (perpendicular to the TI sample) and $\theta = \pi/2$ (parallel to the TI sample), a type of experiment which may prove useful for checking systematically the effects from the TI sidewalls. In both panels the sample width is held fixed at $L_x = 1$, the sample is thin with height $L_y = L_x/10$, and the scattering length is $L_x/100$. In panel 8a we keep the magnetic field fixed at $L_B = 0.1L_x$ and choose four values of the coherence length $L_\phi^2 = [0.01, 0.1, 1, 10]\,L_x^2$. In all cases we find that in-plane magnetoconductivity $\sigma_{WAL}(B)$ is non-zero. In fact the reduction from $\theta = 0$ to $\theta = \pi/2$ is only a factor of 9 when $L_\phi = L_x/10$, and a factor of 3 when $L_\phi = \sqrt{10}L_x$. Significantly, the factor of 9 is close to the ratio of the sample's height to width $L_y/L_x = 10$. In panel 8b we keep $L_\phi = L_x/\sqrt{10}$ and move L_B progressively from the strong field regime (at the bottom of the figure) to the weak field field regime (at the top), i.e $L_B = L_x \times \left[\sqrt{0.01}, \sqrt{0.1}, 1, \sqrt{10}, \sqrt{100}\right]$. Again the ratio of in-plane signal to perpendicular signal is comparable to L_y/L_x, with values ranging from 40 at large fields to 6 at small fields. In the weak-field regime where $L_B \geq L_\phi = L_x/\sqrt{10}$, i.e. the upper four curves, we find that all four curves run in parallel. This is because here the signal is proportional to B^2. The same parallel behavior is visible in the upper two curves of panel 8a.

These numerical results may explain why sizable in-plane signals have been observed repeatedly in TI experiments. Our results indicate that when L_ϕ/L_r is small the ratio of in-plane to perpendicular field signals is roughly L_y/L_x, and in the other cases the ratio is even larger.

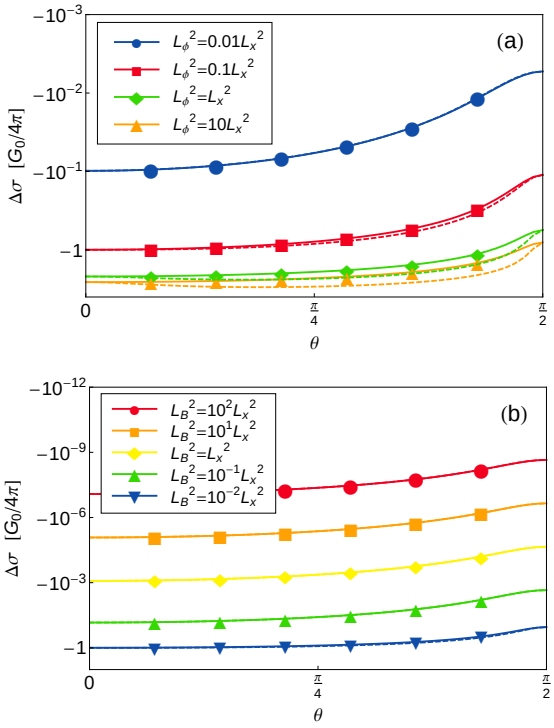

FIG. 8: (Color online.) Dependence on the angle of the magnetic field in a thin sample with height $L_y = L_x/10$. $\theta = 0$ for perpendicular fields and $\theta = \pi/2$ for in-plane fields. In panel a the magnetic field is kept fixed, and in panel b the dephasing length L_ϕ is kept fixed. In both panels the upper curves lie in the strong-field regime. For comparison purposes, the dashed lines show the sum of the perpendicular $\theta = 0$ and in-plane $\theta = \pi/2$ signals. In all cases the in-plane magnetoconductivity is smaller than the perpendicular value, with ratios ranging from 1/3 to 1/40. This is in sharp contrast with a TI without sidewalls where the in-plane magnetoconductivity would be null, and may explain experimental measurements of in-plane signals.

When L_ϕ/L_x is large, i.e. in the wrapped regime, the ratio of in-plane to perpendicular signals can be quite large, since the relevant interference diagrams wrap around the entire TI sample.

Figure 8 also shows dashed lines, which are the sum of the perpendicular conductivity $\sigma_{perp}(B\cos\theta)$ and the in-plane conductivity $\sigma_{in-plane}(B\sin\theta)$. It is experimentally quite feasible to measure the perpendicular and in-plane conductivities and then compare $\sigma_{perp}(B\cos\theta) + \sigma_{in-plane}(B\sin\theta)$ to the tilted magnetoconductivity $\sigma(B,\theta)$. When there is little coupling between the TI's four faces, the two curves should agree. Figure 8a shows generally good agreement, with significant discrepancies only when the coherence length L_ϕ is comparable to or larger than the sample size, precisely because in this case all four sides are coupled to each other. The maximum discrepancy at $L_\phi^2 = 0.01L_x^2$ is 1.6%, at $L_\phi^2 = 0.1L_x^2$ it grows to 12%, and at $L_\phi^2 = 10L_x^2$ it reaches 45%. These discrepancies are small compared to σ's overall variation with θ. Figure 8b also shows small discrepancies, less than 1% at $L_B^2 \geq L_x^2$, and growing to 13% at $L_B^2 = 0.01L_x^2$. We conclude that $\sigma_{perp}(B\cos\theta) + \sigma_{in-plane}(B\sin\theta)$ is a good predictor of the tilted magnetoconductivity, with almost perfect agreement when L_ϕ is small or L_B is large.

V. CONCLUSIONS

In this article we have made a comprehensive exploration of topological effects on the Weak Antilocalization signal in TI samples with perpendicular, in-plane, and tilted magnetic fields. These results are of interest because they bring to light a new experimentally accessible signal of topological transport. They are also practically useful to experimentalists. Our results will affect interpretation of the magnetoconductivity's magnitude, which is often used to estimate the coupling between a TI's top and bottom surfaces. We also showed that TI sidewalls produce an in-plane magnetoconductivity which may account for experimental observations, and we gave both analytical and numerical predictions for tilted samples that explain experimental observations with in-plane fields.

Acknowledgments

We acknowledge useful discussions with Xi Dai, Yongqing Li, Chaojing Lin, Quansheng Wu, and Hu-Jong Lee. K.B.A. and I.A.S. acknowledge the support of FP7 IRSES project QOCaN. This work was initiated at the Institute of Physics in Beijing, with support from the National Science Foundation of China and the 973 program of China under Contract No. 2011CBA00108.

Appendix A: Analytical Calculation of the Magnetoconductivity

In this appendix we analytically calculate the magnetoconductivity. In the first section we calculate the conductivity from wrapped Cooperon states, which is the full result at small fields. In our finite system the weak-field result is necessarily analytic and even in B^2, as we discuss in the next section. Lastly we calculate the contribution from harmonic oscillator Cooperon states, which becomes important at stronger fields.

We begin by discussing the relevant length scales and expected results. As discussed earlier, our numerical results show that any features scaling with L_ϕ are strongly suppressed or nonexistent in the small samples of interest to

us, where wrapping is important. This is because the wrapping effect requires that L_ϕ be larger than the sample perimeter. As described earlier, we adopt the following prescription for small samples: we replace L_ϕ^2 with a new length scale $L_{\phi r}^2$, given by $L_{\phi r}^{-2} = L_\phi^{-2} + (L_r/2\pi)^{-2}$. This has two main results. Firstly, in small $L_r \ll L_\phi$ samples the L_ϕ length scale is replaced by the sample size $L_r/2\pi$. Secondly, in small samples the magnetoconductivity's dependence on temperature disappears.

1. The Conductivity from Wrapped States - Equal to the Total Conductivity in Weak Fields

As shown in equation 5, our calculation of the magnetoconductivity reduces to a study of the eigenstates and eigenvalues of the Cooperon diffusion operator A which includes a potential representing the magnetic field:

$$\begin{aligned} \langle \sigma_{WAL}(B) \rangle &= \frac{G_0}{4\pi} 2L_{\phi r}^2 \int \frac{dk_z}{L_r} \sum_i^{E_i<E_l} E_i^{-1},\ E_i|i\rangle = A|i\rangle \\ A = & \quad V(r,R_g) - L_{\phi r}^2(\partial/\partial_r)^2 + 1,\ V(r,R_g) = (L_{\phi r}^2/L_B^4)(R(r) + L_B^2 k_z)^2 \end{aligned} \tag{A1}$$

The function $R(r)$ figuring in the potential was specified earlier. The average value of $V(r,R_g)$ is $\langle V \rangle = L_{\phi r}^2 k_z^2 + \gamma$, $\gamma = L_{\phi r}^2 \langle R^2(r) \rangle / L_B^4$. $\langle R^2(r) \rangle$ is the second moment of $R(r)$, scales quadratically with the perimeter L_r, and is given in equation 6.

In this section we concentrate on the contribution from wrapped Cooperon states, which can be analytically continued to $B = 0$ where they are plane waves. In general, the conductivity includes contributions from wrapped, sidewall, edge, and harmonic oscillator states. However at weak enough field strength the potential is not strong enough to generate any bound states, and all eigenstates and eigenvalues can be analytically continued to $B = 0$; all Cooperon eigenstates are wrapped states. (This is not true in an infinite system, where at any $B \neq 0$ the spectrum is broken into equally spaced Landau levels.) In other words, at weak enough fields the potential $V(r,R_g)$ is not strong enough to create any bound states; therefore there is no contribution to the conductivity from sidewall, edge, or harmonic oscillator states.

The most obvious approximation for calculating the wrapped Cooperon state contribution is the Virtual Crystal Approximation,[47,48] which simply takes the average of the potential and obtains

$$E_i = 1 + L_{\phi r}^2 k_r^2 + \langle V \rangle \tag{A2}$$

$k_r = n_r 2\pi/L_r$ is the wave-number of the plane wave. This approximation simply shifts the plane-wave eigenvalues by a dimensionless constant $\gamma = L_{\phi r}^2 \langle R^2(r) \rangle / L_B^4$, and the magnetic field's effect is controlled completely by this constant. This approximation is closely linked to the magnetic phase relaxation approximation, which estimates the lowest excitation energy δE of the Cooperon's ground state, and adds this E_i.[49,50] The $\langle V \rangle$ term appearing in equation A2 is the VCA approximation's estimate of the shift δE of the Cooperon's lowest excitation energy.

The remaining integral is easy because we have preserved rotational symmetry; we obtain

$$\begin{aligned} \langle \sigma_{WAL}(B) \rangle &= \frac{G_0}{4\pi} (\ln|E_l| - \ln|1+\gamma|) \\ \langle \Delta\sigma_{WAL}(B) \rangle &= -\frac{G_0}{4\pi} \ln|1+\gamma|,\ \gamma = L_{\phi r}^2 \langle R^2(r) \rangle / L_B^4 \end{aligned} \tag{A3}$$

This formula is illustrated in Figure 9b, which uses identical parameters to those used in Figure 4. In the wrapped regime where the coherence length is much larger than the sample size $L_\phi \gg L_r$, the γ parameter scales with $(L_r/L_B)^4$. In this regime the magnetoconductivity is quadratic at small fields and transitions to logarithmic behavior at $L_B \propto L_r$. Qualitatively this is the correct behavior. However comparison with Figure 4 shows that at small fields the Virtual Crystal Approximation systematically overestimates the magnetoconductivity. Moreover it does not capture the correct physics at field strengths which are intermediate between $L_B \propto L_r$ and the wrapping transition which occurs at much bigger fields where $L_B \propto \sqrt{lL_r}$. In this transition region the Virtual Crystal Approximation predicts logarithmic growth, while our numerical results show much faster growth, closer to a power law. The reason for this discrepancy is that the Virtual Crystal Approximation neglects the conversion from wrapped states to bound states, i.e. to sidewall and harmonic oscillator states.

a. Derivation of the Virtual Crystal Approximation from Perturbation Theory

Here we do a correct perturbative expansion to second order in the magnetic field $B \propto x \propto 1/L_B^2$. At zeroth order we have $V(r,R_g) = L_{\phi r}^2 k_z^2$, and added to this is the perturbation $\delta V = 2(L_{\phi r}^2/L_B^2) k_z R(r) + L_{\phi r}^2 R^2(r)/L_B^4$.

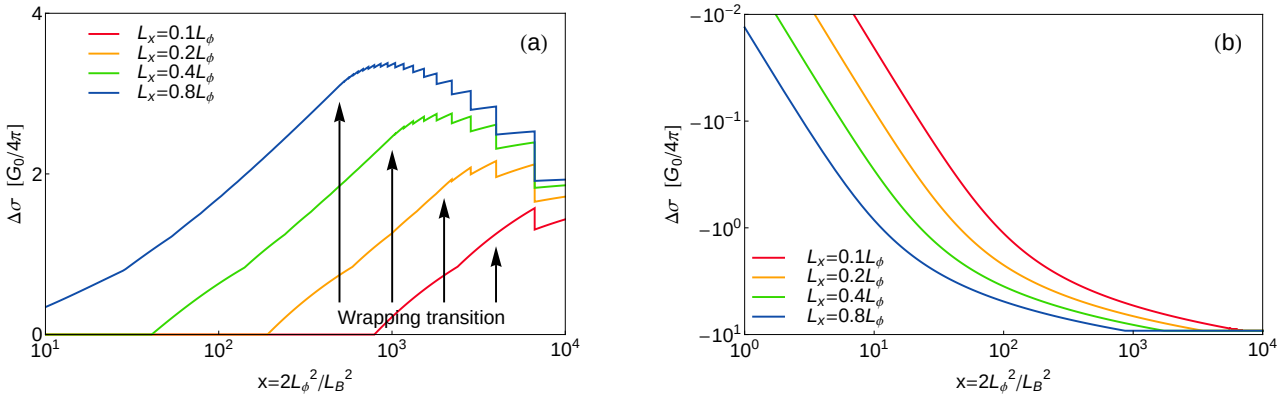

FIG. 9: (Color online.) Analytical Theory of the Wrapped Magnetoconductivity. For easy comparison with Figure 4, here all parameters and scales are identical to those used in Figure 4. Pane a shows the contribution from harmonic oscillator bound states. Inside the wrapping transition this contribution increases with B because B causes more bound states. At the wrapping transition this trend reverses as the increasing bound state energies begin to cross the high-energy cutoff associated with the scattering length l. The logarithmic decrease seen here at large fields is responsible for the identical feature in the HLN formula. Pane b shows the contribution from wrapped states. At small fields we find the usual quadratic behavior, with a transition to logarithmic growth when when L_B is proportional to the sample size.

Perturbation theory states that at second order in V the energy is

$$E_i \;=\; 1 + L_{\phi r}^2 k_z^2 + L_{\phi r}^2 k_r^2 + \langle k_r|\delta V|k_r\rangle + \sum_{j\neq n_r} \frac{|\langle k_r|\delta V|k_j\rangle|^2}{L_{\phi r}^2(k_r^2 - k_j^2)} \tag{A4}$$

If we omit the last term we obtain the Virtual Crystal Approximation, because $\langle n_r|\delta V|n_r\rangle = \gamma$. Keeping only terms of order $O(B^2)$ and simplifying produces the following result:

$$E_i \;=\; 1 + L_{\phi r}^2 k_z^2 (1 + L_B^{-4}\lambda^4(k_r)) + L_{\phi r}^2 k_r^2 + \gamma,\; \lambda^4(k_r, L_x, L_y, l) = 4 \sum_{k_j\neq n_r} \frac{|\langle k_r|R(r)|k_j\rangle|^2}{k_r^2 - k_j^2} \tag{A5}$$

This result is exact up to second order in B, as long as the sample is finite. Its most interesting feature is the emergence of a new dimensionless parameter, λ^4/L_B^4, which is completely independent of the dephasing length $L_{\phi r}$ and of temperature. λ^4 cannot be larger than $O(L_r^4)$, and may be as small as $O(L_r^2 a^2)$. We should note that the sign of λ^4 is not fixed a priori, and is guaranteed to be negative when $k_r = 0$; we used this notation only to point out the emergence of a new length scale.

This result leads us to expect that at small B the magnetoconductivity is subject to competition between on one hand $L_{\phi r}^2 L_r^2/L_B^4$ and on the other hand the temperature-independent ratio λ^4/L_B^4. In small samples the former scales with L_r^4/L_B^4. The latter is bounded above by the same quantity, but may be as small as $L_r^2 a^2/L_B^4$.

In the wrapped regime $\gamma \propto L_r^4$. The λ^4 term cannot scale faster than this and may have a much slower scaling, which justifies its omission and the use of the Virtual Crystal Approximation.

2. Can the Magnetoconductivity Contain Terms that are Odd in B?

It is of considerable interest to understand whether the magnetoconductivity may have terms that are linear in $B \propto x$ at small B. In our equation 5 for the magnetoconductivity the integration $x\, dR_g$ is independent of B, and x figures only in the potential $V(r, R_g)$. Within the potential, the linear part is is $-2(x^2/4L_{\phi r}^2)R_g\, R(r) = xR(r)\, k_z$. We will now show that if we do perturbation theory in this linear part, every term which is odd in $B \propto x$ will be exactly zero.

We obtain this result by noticing that the potential for our square TI sample shows a discrete symmetry: it is unchanged if it reverses sign and is shifted by $r \to r + L_x + L_y$. Another way of saying this is that the $xR(r)\, k_z$ term mirrors itself - with opposite sign - under translation by $L_x + L_y$. Since neither copy is preferred, odd powers of $xR(r)\, k_z$ must integrate to zero, and the magnetoconductivity cannot contain odd powers of B.

More generally, in the original formulation with $\vec{\nabla} - \imath 2e\vec{A}/\hbar$, if the geometry (without a magnetic field) retains symmetry under $\vec{x} \to -\vec{x}$ then odd powers of $B \propto x$ are prohibited.

This argument does not exclude the possibility of non-analytic terms which are linear in B, associated with a failure of perturbation theory. Such terms could appear if an infinitely small linear term generates new bound states that cannot be analytically continued to $B = 0$, or if the density of states changes discontinuously at $B = 0$. In our problem with a simple magnetic field this can occur only if the system is infinite. In that case the eigenvalues $E_n = |x|(n+1/2)$ are those of the simple harmonic oscillator; they are linear in B, and are non-analytic when B changes sign.

3. The Harmonic Oscillator Conductivity

In the following we estimate the contribution from harmonic oscillator Cooperon states. We assume that the magnetic field is perpendicular to the TI. If the energy E_n is small enough that the eigenfunction is trapped on one face of the TI, i.e. both turning points lie on that face, then the bound state eigenvalues coincide with those of the harmonic oscillator: $E_n^{HO} = 1 + (n + 1/2)x|\frac{dR(r)}{dr}|$. Therefore the conductivity is:

$$\begin{aligned}
\langle\sigma_{WAL}(B)\rangle &= 2 \times G_0 \frac{L_{\phi r}^2}{2\pi x} \int_{-L_x/2L_B^2}^{L_x/2L_B^2} \frac{dk_z}{L_r} \sum_{n=0}^{1+(n+1/2)x<min(E_l,1+\xi^2(1-|r|)^2/4)} (1/x + (n+1/2))^{-1} \\
&= G_0 \frac{1}{4\pi} \frac{2L_x}{L_r} \int_0^1 dr \sum_{n=0}^{1+(n+1/2)x<min(E_l,1+\xi^2(1-r)^2/4)} (1/x + (n+1/2))^{-1} \\
&= G_0 \frac{1}{4\pi} \frac{2L_x}{L_r} \sum_{n=0}^{1+(n+1/2)x<min(E_l,1+\xi^2/4)} \int_0^{1-2\sqrt{(n+1/2)x}/\xi} dr\ (1/x + (n+1/2))^{-1} \\
&= G_0 \frac{1}{4\pi} \frac{2L_x}{L_r} \sum_{n=0}^{1+(n+1/2)x<min(E_l,1+\xi^2/4)} \frac{1 - 2\sqrt{(n+1/2)x}/\xi}{1/x + n + 1/2} \\
r &= -2k_z L_B^2/L_x,\ \xi = L_{\phi r} L_x / L_B^2 = x L_x / 2L_{\phi r}
\end{aligned} \tag{A6}$$

The factor of 2 in the initial formula occurs because we are counting states from both the top and bottom faces of the TI. The limits of integration $\pm L_x/2L_B^2$ are the values of k_z where the quadratic sections of the potential $V(R_g, r)$ cease to have minima. The factor of $\xi^2(1 - |r|)^2/4$ in the sum's upper limit is the lower of $V(R_g, r)$'s two values at the sidewalls where $\pm L_x/2$.

This formula is plotted in Figure 9a, with the same parameters used in our numerical calculations shown in Figure 4. At large fields, i.e. outside the wrapping transition, all states are harmonic oscillator and sidewall bound states, and in thin samples the harmonic oscillator states are dominant. Therefore our harmonic oscillator formula is nearly exact at large fields, and in particular reproduces the correct logarithmic decrease. At smaller fields below the wrapping transition at $L_B \propto \sqrt{L_r l}$ the potential becomes too weak to trap any bound states, and the harmonic oscillator contribution disappears, as shown in Figure 9a. Our formula also shows the position of the wrapping transition.

The physics at smaller fields inside the wrapping transition involves a nonperturbative transformation of the states and their spectrum from harmonic oscillator states, to sidewall bound states, to finally unbound wrapped states which can be analytically continued to plane waves. Our formula omits all details of this process, so our formula is inaccurate inside the wrapping transition. Neither the Virtual Crystal Approximation nor the harmonic oscillator contribution, nor their combination, is able to give a qualitatively adequate picture of intermediate field strengths between $L_B \propto L_r$ and $L_B \propto \sqrt{L_\phi L_r}$.

4. Summary of our Analytical Results

In this appendix we have calculated the contributions from wrapped and harmonic oscillator Cooperon states to the quantum conductivity $\langle\sigma_{WAL}(B)\rangle$. The harmonic oscillator formula shows the wrapping transition and gives the correct strong-field logarithmic behavior. At small fields the wrapped contribution is equal to the total signal. We developed the Virtual Crystal Approximation which gives a qualitatively correct picture of the weak-field quadratic region, and of the transition at stronger fields $L_B^2 < L_x^2/2$. It also informed us of the signal's dependence on $\gamma = L_{\phi r}^2 \langle R^2(r)\rangle / L_B^4$, which this article's main body showed is important for understanding the effects of changing the sample height, and of changing the temperature.

* Electronic address: vincent@sacksteder.com; Vincent Sacksteder previously worked at the Institute of Physics, Chinese Academy of Sciences, Beijing 100190, China, where this work was begun.

[1] C. L. Kane and E. J. Mele, Physical Review Letters **95**, 226801 (2005).

[2] H. Min, J. E. Hill, N. A. Sinitsyn, B. R. Sahu, L. Kleinman, and A. H. MacDonald, Physical Review B **74**, 165310 (2006).

[3] H. Zhang, C.-X. Liu, X.-L. Qi, X. Dai, Z. Fang, and S.-C. Zhang, Nature Physics **5**, 438 (2009).

[4] M. Z. Hasan and C. L. Kane, Reviews of Modern Physics **82**, 3045 (2010).

[5] D. Culcer, Physica E **44**, 860 (2012).

[6] J. H. Bardarson and J. E. Moore, Reports on Progress in Phyiscs **76**, 056501 (2013).

[7] P. M. Ostrovsky, I. V. Gornyi, and A. D. Mirlin, Physical Review Letters **98**, 256801 (2007).

[8] K. Nomura, M. Koshino, and S. Ryu, Physical Review Letters **99**, 146806 (2007).

[9] E. R. Mucciolo and C. H. Lewenkopf, J. Phys.: Condens. Matter **22**, 273201 (2010).

[10] Q. Wu and V. E. Sacksteder, arXiv preprint arXiv:1309.6738 (2013).

[11] J. Chen, H. J. Qin, F. Yang, J. Liu, T. Guan, F. M. Qu, G. H. Zhang, J. R. Shi, X. C. Xie, C. L. Yang, et al., Physical Review Letters **105**, 176602 (2010).

[12] Y. Q. Li, K. H. Wu, J. R. Shi, and X. C. Xie, Front. Phys. **7**, 165 (2012).

[13] S. Hikami, A. I. Larkin, and Y. Nagaoka, Prog. Theor. Phys. Progress Letters **63**, 707 (1980).

[14] J. Chen, X. Y. He, K. H. Wu, Z. Q. Ji, L. Lu, J. R. Shi, J. H. Smet, and Y. Q. Li, Physical Review B **83**, 241304 (2011).

[15] H. Steinberg, J.-B. Laloë, V. Fatemi, J. S. Moodera, and P. Jarillo-Herrero, Physical Review B **84**, 233101 (2011).

[16] I. Garate and L. Glazman, Physical Review B **86**, 035422 (2012).

[17] B. Al'tshuler, A. Aronov, and B. Spivak, JETP Lett **33**, 94 (1981).

[18] A. Aronov and Y. V. Sharvin, Reviews of modern physics **59**, 755 (1987).

[19] H. Peng, K. Lai, D. Kong, S. Meister, Y. Chen, X.-L. Qi, S.-C. Zhang, Z.-X. Shen, and Y. Cui, Nature materials **9**, 225 (2010).

[20] F. Xiu, L. He, Y. Wang, L. Cheng, L.-T. Chang, M. Lang, G. Huang, X. Kou, Y. Zhou, X. Jiang, et al., Nature nanotechnology **6**, 216 (2011).

[21] A. Sulaev, P. Ren, B. Xia, Q. H. Lin, T. Yu, C. Qiu, S.-Y. Zhang, M.-Y. Han, Z. P. Li, W. G. Zhu, et al. (2013).

[22] J. Dufouleur, L. Veyrat, A. Teichgräber, S. Neuhaus, C. Nowka, S. Hampel, J. Cayssol, J. Schumann, B. Eichler, O. Schmidt, et al., Physical review letters **110**, 186806 (2013).

[23] B. L. Altshuler and A. G. Aronov, JETP Letters **33**, 499 (1981).

[24] V. Dugaev and D. Khrnel'nitskii, Zh. Eksp. Teor. Fiz **86**, 1784 (1984).

[25] C. W. J. Beenakker and H. Van Houten, Physical Review B **38**, 3232 (1988).

[26] G. Tkachov and E. Hankiewicz, physica status solidi (b) **250**, 215 (2013).

[27] O. Raichev and P. Vasilopoulos, Journal of Physics: Condensed Matter **12**, 589 (2000).

[28] H.-T. He, G. Wang, T. Zhang, I.-K. Sou, G. K. L. Wong, J.-N. Wang, H.-Z. Lu, S.-Q. Shen, and F.-C. Zhang, Physical Review Letters **106**, 166805 (2011).

[29] Y. Zhao, C.-Z. Chang, Y. Jiang, A. DaSilva, Y. Sun, H. Wang, Y. Xing, Y. Wang, K. He, X. Ma, et al., Scientific Reports **3**, 3060 (2013).

[30] C. Lin, X. He, J. Liao, X. Wang, V. Sacksteder IV, W. Yang, T. Guan, Q. Zhang, L. Gu, G. Zhang, et al., Physical Review B **88**, 041307 (2013).

[31] X. Wang, X. He, T. Guan, J. Liao, C. Lin, K. Wu, Y. Li, and C. Zeng, Physica E: Low-dimensional Systems and Nanostructures **46**, 236 (2012).

[32] J. Lee, J. Park, J.-H. Lee, J. S. Kim, and H.-J. Lee, Physical Review B **86**, 245321 (2012).

[33] J. J. Cha, D. Kong, S.-S. Hong, J. G. Analytis, K. Lai, and Y. Cui, Nano Letters **12**, 1107 (2012).

[34] P. Gehring, H. M. Benia, Y. Weng, R. Dinnebier, C. R. Ast, M. Burghard, and K. Kern, Nano Letters **13**, 1179 (2013).

[35] T. Chen, Q. Chen, K. Schouteden, W. Huang, X. Wang, Z. Li, F. Miao, X. Wang, Z. Li, B. Zhao, et al., arXiv.org **arXiv:1401.0383v1** (2014).

[36] V. E. Sacksteder, S. Kettemann, Q. S. Wu, X. Dai, and Z. Fang, Physical Review B **85**, 205303 (2012).

[37] G. Bergmann, Physical Review B **39**, 11280 (1989).

[38] V. Sacksteder and X. Dai, in preparation.

[39] S. Maekawa and H. Fukuyama, Journal of the Physical Society of Japan **50**, 2516 (1981).

[40] P. A. Lee and T. Ramakrishnan, Reviews of Modern Physics **57**, 287 (1985).

[41] B. Altshuler, A. Aronov, and A. Y. Zuzin, Solid State Communications **44**, 137 (1982).

[42] A. Sahnoune, J. O. Ström-Olsen, and H. E. Fischer, Physical Review B **46**, 10035 (1992).

[43] J. Rammer, *Quantum transport theory* (Westview Press, 2004).

[44] E. McCann, K. Kechedzhi, V. I. Falko, H. Suzuura, T. Ando, and B. L. Altshuler, Physical review letters **97**, 146805 (2006).

[45] F. Zhang, C. L. Kane, and E. J. Mele, Physical Review B **86**, 081303 (2012).

[46] P. G. Silvestrov, P. W. Brouwer, and E. G. Mishchenko, Physical Review B **86**, 075302 (2012).

[47] L. Nordheim, Ann. Phys. (Leipzig) **9**, 607 (1931).

[48] T. Muto, Sci. Pap. Inst. Phys. Chem. Res. (Jpn.) **34**, 377 (1938).

[49] S. Kettemann and R. Mazzarello, Physical Review B **65**, 085318 (2002).

[50] S. Kettemann, Physical review letters **98**, 176808 (2007).

[51] Y. V. Sharvin, Physica B **126**, 288 (1984).

[52] If we had included the three spin triplet states in our calculation of σ_{WAL}, then $\Gamma(B)$ would be a 4×4 operator acting on the space of spin singlet and spin triplet states, and σ_{WAL} would be determined by Γ's trace. Because the spin triplet has short decay times, its contribution to $\Gamma(B)$'s trace is small.

[53] The sensitivity to the system width was known to Altshuler and Sharvin, who included it in their calculation of the ef-

fect of a small perpendicular field on AAS oscillations.[18,51]